Chandra and *XMM* monitoring of the black hole X-ray binary IC 10 X-1

Silas G. T. Laycock,★ Rigel C. Cappallo and Matthew J. Moro

Department of Physics and Applied Physics, Olney Science Center, University of Massachusetts, Lowell, MA 01854, USA

ABSTRACT

The massive black hole (BH)+Wolf–Rayet (WR) binary IC 10 X-1 was observed in a series of 10 *Chandra* and two *XMM–Newton* observations spanning 2003–2012, showing consistent variability around 7×10^{37} erg s^{-1}, with a spectral hardening event in 2009. We phase connected the entire light curve by folding the photon arrival times on a series of trial periods spanning the known orbital period and its uncertainty, refining the X-ray period to $P = 1.45175(1)$ d. The duration of minimum flux in the X-ray eclipse is ∼5 h which together with the optical radial velocity (RV) curve for the companion yields a radius for the eclipsing body of 8–10 R$_\odot$ for the allowed range of masses. The orbital separation $(a_1 + a_2) = 18.5$–22 R$_\odot$ then provides a limiting inclination $i > 63°$ for total eclipses to occur. The eclipses are asymmetric (egress duration ∼0.9 h) and show energy dependence, suggestive of an accretion disc hotspot and corona. The eclipse is much (∼5×) wider than the 1.5–2 R$_\odot$ WR star, pointing to absorption/scattering in the dense wind of the WR star. The same is true of the close analog NGC 300 X-1. RV measurements of the He II [$\lambda\lambda 4686$] line from the literature show a phase shift with respect to the X-ray ephemeris such that the velocity does not pass through zero at mid-eclipse. The X-ray eclipse leads inferior conjunction of the RV curve by ∼90°, so either the BH is being eclipsed by a trailing shock/plume, or the He II line does not directly trace the motion of the WR star and instead originates in a shadowed partially ionized region of the stellar wind.

Key words: binaries: eclipsing – stars: black holes – stars: Wolf–Rayet – X-rays: binaries.

1 INTRODUCTION

The extragalactic X-ray binary IC 10 X1 consists of a black hole (BH) and a Wolf–Rayet (WR) star orbiting their common centre of mass with a period of 34.9 h. X-ray timing and optical radial velocity (RV) studies (Prestwich et al. 2007; Silverman & Filippenko 2008) have determined a range of dynamically allowable masses for the two objects. The lowest mass scenario is $M_\star = 17$ M$_\odot$, $M_{BH} = 23$ M$_\odot$, and the most massive scenario is $M_\star = 35$ M$_\odot$, $M_{BH} = 32$ M$_\odot$. These configurations follow from the characterization of the WR star by Clark & Crowther (2004) and the mass function determined from the RV curve of the primary (Silverman & Filippenko 2008). Deep eclipses are seen in the X-ray light curve as was first noted by Prestwich et al. (2007), who confirmed this fact with a 10 d series of *Swift* observations in 2006. The system resides in the nearby dwarf starburst galaxy IC 10 at a distance of 660 kpc (Wilson et al. 1996).

In this paper we describe the X-ray properties of IC 10 X-1 over the period 2003–2014, focusing on the *Chandra* data set, and incorporate the *XMM–Newton* broad-band light curves in order to extend the duration of the time series.

IC 10 X-1 belongs to the small group of known black hole high-mass X-ray binaries (BH-HMXBs), which includes Cyg X-1 (Bolton 1972; Hutchings et al. 1973), Cyg X-3 (Hanson, Still & Fender 2000), Large Magellanic Cloud (LMC) X-1 (Orosz et al. 2009), LMC X-3 (Nowak et al. 2001), M33 X-7 (Orosz et al. 2007), NGC 300 X-1 (Carpano et al. 2007; Crowther et al. 2010; Binder et al. 2011), and CXOU J123030.3+413853 in NGC 4490 (Esposito et al. 2013). We note the incidence of apparently eclipsing systems is surprisingly high among BH-HMXBs.

The majority of known stellar BHs and candidate systems are in low-mass systems (low-mass X-ray binaries, LMXBs), probably because the lifetimes of lower mass donor stars are longer. In contrast, the most massive stellar BHs appear to have the most massive companions; the current record holders are M33 X-7 (a 70 M$_\odot$ O-star) and IC 10 X-1 (Valsecchi et al. 2010). This phenomenon that has been investigated by de Mink et al. (2010) who show that rapid rotation and tidally induced mixing between the core and envelope alters the evolution of extremely massive binary stars in an interesting way. The companion avoids the red giant phase and evolves directly to massive helium star (effectively a WR star), retaining a much higher mass, and a more compact size than in the isolated case. Detailed binary evolutionary scenarios have been explored by Bogomazov (2014) who note that their birth events are leading candidates for long gamma-ray bursts (GRBs), and that BH-HMXBs'

eventual fate as BH+BH binaries will be a significant source of gravitational wave radiation. We suggest Remillard & McClintock (2006) and Frolov & Zelnikov (2011) for comprehensive reviews of observations and theory of BH X-ray binaries.

A key goal in this study was to refine the binary period to the point that its derivative ($\dot{P}$) could be tracked by future observations. The rate at which the orbital period changes ($\frac{\dot{P}}{P}$) is a crucial parameter in BH binary systems, as it contains measurable contributions from gravitational radiation, magnetic braking, and mass loss from the primary (González Hernández, Rebolo & Casares 2014). Fundamental research in general relativity and particle physics requires more such measurements; for example Johannsen (2009) shows that $\dot{P}$ in BH binaries provides one of the only experimental constraints on the properties of extra dimensions predicted by string theory. Evolutionary simulations of BH-HMXBs by Tutukov, Fedorova & Cherepashchuk (2013) suggest that experimental determination of $\frac{\dot{P}}{P}$ in IC 10 X-1 is the most promising route to understand the relationship between the companion's wind properties and the X-ray luminosity.

Improving the orbital ephemeris is crucial for other reasons too. First, for interpretation of the existing data it is necessary to know the orbital phase; for example to generate the eclipse profile, or to compare the spectrum in and out of eclipse. Secondly, no existing RV studies for IC 10 X-1 and NGC 300 X-1 have explicitly demonstrated that the He II λλ4686 emission line shift passes through zero at X-ray minimum (Tutukov et al. 2013). The He II line emission used to obtain the RV curve is probably inhomogeneous and variable, hence it is not certain that the RV curves of the optical stars in these systems accurately reflect their orbital motions.

The X-ray spectrum of IC 10 X-1 has been characterized from *XMM–Newton* and *Chandra* observations of 2003 by Wang, Whitaker & Williams (2005) and Bauer & Brandt (2004). Both groups found a spectrum that is similar to other BH-HMXBs, exhibiting a hard accretion disc component embedded in a softer thermal extended emission.

In all published light curves of X1 the source exhibit flaring on time-scales of minutes to hours, and several observations show slower variations which are likely segments of eclipse ingress/egress, but could plausibly be due to variations in the mass transfer rate. A ∼7 mHz quasi-periodic oscillation (QPO) has been discovered in the X-ray light curve by Pasham, Strohmayer & Mushotzky (2013). Its frequency is similar to that seen in highly inclined X-ray binaries; in which the accretion disc obscures the central source leading to so-called dipping behaviour. Alternatively 'heartbeat' QPOs due to radiation pressure instability of the inner edge of the accretion disc can also appear in the same frequency range. Differentiation of these models could come from additional QPO measurements as the system transitions to different accretion states. Luminosity variations occur in BH-HMXBs on all timescales, as is seen in for example Cyg X-1 (Grinberg et al. 2014), thus establishing the long-term activity of IC 10 X-1 and occurrence of state transitions is essential to understanding the stability of its accretion geometry.

2 OBSERVATIONS AND DATA REDUCTION

IC 10 has been observed by *Chandra* 10 times and twice by *XMM–Newton* as listed in Table 1. The monitoring series of seven observations (late 2009 through 2010) were intended to fill-in the phase coverage of IC 10 X-1's orbit, extend the baseline in order to refine the orbital period, and search for transient X-ray sources (Laycock et al. 2010; Laycock & Cappallo 2014). *Chandra* data re-

Table 1. X-ray observations of IC 10 X-1.

MJD	Date	Inst.	ObsID	Offset (arcmin)	Exp (ks)	Cts (×10³)
52710.7	12 March 2003	*CXO*	03953	0.48	28.9	5.21
52823.9	2 July 2003	*XMM*	152260	0.02	42	21
54041.8	2 Nov 2006	*CXO*	07082	3.20	40.1	3.75
54044.2	5 Nov 2006	*CXO*	08458	3.20	40.5	4.58
55140.7	5 Nov 2009	*CXO*	11080	1.90	14.6	0.54
55190.2	25 Dec 2009	*CXO*	11081	1.74	8.1	0.9
55238.5	11 Feb 2010	*CXO*	11082	0.83	14.7	2.14
55290.6	4 April 2010	*CXO*	11083	2.25	14.7	2.33
55337.8	21 May 2010	*CXO*	11084	3.45	14.2	0.56
55397.5	20 July 2010	*CXO*	11085	2.27	14.5	0.34
55444.6	5 Sep 2010	*CXO*	11086	2.22	14.7	2.26
56157.9	18 Aug 2012	*XMM*	693390	0.01	135	48.6

Notes. Instrument is *Chandra* ACIS-S3 or *XMM–Newton* PN. Cts is net background subtracted counts.

duction was performed in CIAO[1] following the standard processing threads for point sources. The *Chandra* Advanced CCD Imaging Spectrometer-S-array (ACIS-S) Level-2 event files were barycentre corrected with ABARY to remove timing artefacts due to Earth's motion around the Sun. For the declination of IC 10 (+59°.3) the annual path length variation is ±254 light-seconds. Source fluxes were computed in three bands (broad-band $B = 0.3$–8 keV, soft band $S = 0.1$–1.5 keV, and hard band $H = 5.0$–10 keV) from WAVDETECT output, and the same bands were used to generate light curves and hardness ratios (HRs). Event files were extracted for the source using the 95 per cent encircled energy radius. Background events were extracted in an annulus bounded by the corresponding 3σ and 4σ radii. Exposure maps generated for 1.5 keV were used to correct for sensitivity variations.

Source and background spectra with region-specific response files (RMF, ARF) were created using the CIAO script SPECEXTRACT for each observation. The data and response files were analysed in XSPEC 12.7.[2]

Further analysis of all light curves and events was performed in R.[3]

XMM–Newton light curves were obtained from the standard pipeline products in the *XMM–Newton* Science Archive (XSA)[4]. We used the background corrected broad-band PN light curve at 40 s time resolution barycentre corrected for the Earth's motion.

3 LIGHT CURVES: FLUX AND HARDNESS RATIO VARIABILITY

X1 is detected in all 10 observations of IC 10, and the resulting long-term light curve from *Chandra* and *XMM–Newton* is plotted in Fig. 1. The *Chandra* count rates (CRs) have been corrected for exposure time, exposure map (i.e. spatial location on the detector), and changes in detector sensitivity with time. The *XMM–Newton* points have been converted to the same flux scale as *Chandra* using WEBPIMMS. The observations vary in integration time (Table 1) and the intrinsic source flux varies significantly during each exposure. The solid points in the long-term light curve are the average flux measured during each observation, the range of variability is shown

[1] http://cxc.harvard.edu/ciao
[2] http://heasarc.nasa.gov/xanadu/xspec
[3] The R Project for Statistical Computing (www.r-project.org).
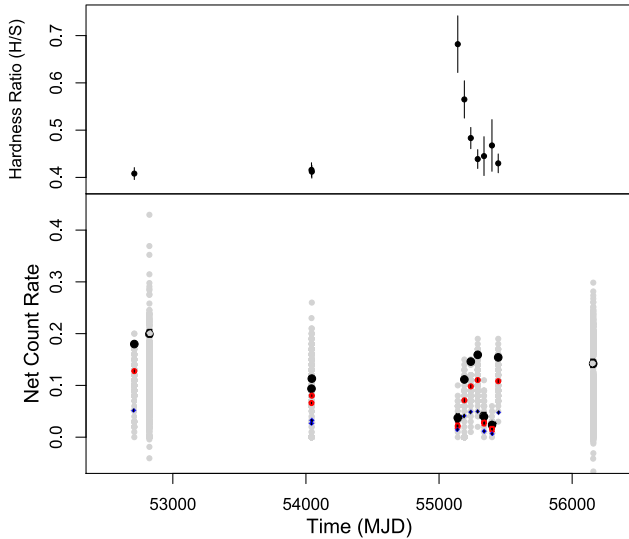[4] 4http://xmm.esac.esa.int/xsa/

Figure 1. Long-term X-ray light curve and HR for IC 10 X-1. Lower panel: average *Chandra* ACIS-S CRs for each observation are plotted in three energy bands: $B = 0.3$–8 keV (black), $S = 0.3$–1.5 keV (red), and $H = 2.5$–8 keV (blue). The two *XMM–Newton* PN measurements (open circles) were translated to the ACIS-S *B* band using PIMMS. During all observations the CR varied strongly due to a combination of eclipses and flaring, this is indicated by the grey points which are broad-band values obtained at 100 s resolution during each observation. Upper panel: hardness ratio (H/S) for the ACIS-S observations with statistical error bars.

by light grey dots. The broad-band CRs in Fig. 1 show a factor of ∼4 variability both between and within observations. The variability contains contributions from eclipses, intrinsic source variability (flickering), and possibly changes in accretion rate and geometry.

The HRs (H/S) reveal that a change in spectral shape took place during the 2009–2010 monitoring series. Over the course of four observations the HR dropped from a peak of 0.68 ± 0.06 back to 0.44 ± 0.02, which is consistent with its prior (2003, 2006) value of 0.41 ± 0.015. The peak value is an increase of 67 per cent over the baseline value, while at the same time the amplitude of the short-term (intraobservation) flux variability appears to shrink.

We examined variability within each *Chandra* observation by plotting broad-band CR and HR at 500 s resolution, as displayed in Fig. 2. The most obvious features are the eclipse egress and ingress caught in observations 2 and 3. Even during eclipse the broad-band flux does not drop to zero, and variability is always present. This suggests that the emission region is not fully eclipsed and that the emission is not point-like. A point source undergoing eclipses produces an instantaneous change in flux, whereas the *Chandra* CR in Fig. 2 (panels 2 and 3) takes 1–2 h to fully transition.

Within all observations the HR fluctuates by a smaller proportion than the broad-band CR. Most of the time the HR appears generally positively correlated with CR, such as in *Chandra* observations 6, 7, and 8. At other times large changes appear in the CR that do not register in HR (e.g. the entire latter half of observation 2), or appear only as features of much shorter duration; for example 3/4 of the way through observation 1.

The correlation between HR and CR was investigated by plotting the X-ray colour–magnitude diagram (CMD; CR versus HR) in Fig. 3. This reveals a split between high and low flux states, which occurs at a CR of 0.06 counts s^{-1}, corresponding to a luminosity of 4×10^{37} erg s^{-1} (assuming $D_{IC 10} = 600$ kpc, and a power-law spectrum with $\Gamma = 1.5$, $N_H = 5 \times 10^{21}$). This CR also happens to divide

the eclipse and uneclipsed CR values seen in observations 2 and 3. Interestingly, observations 4, 8, and 9 all lie completely below the 0.06 counts s^{-1} threshold. The full duration of X1's eclipses is about 7 h, with 5 h spent at minimum flux. The monitoring observations are all <15 ks (a similar duration to the eclipses) so it is possible that the three low flux observations are all 'in eclipse', since the odds of a single observation falling mid-eclipse is about 14 per cent (5/35). During the eclipse egress of ObsID 07082 (Fig. 2, panel 3) the HR is seen to rise steadily, Fig. 4 shows the events binned at 5000 s intervals to improve the signal-to-noise ratio (S/N), demonstrating that the eclipse profile is energy dependent. Curiously the rise in HR *precedes* the corresponding rise in flux that signals egress.

4 REFINING THE ORBITAL PERIOD

Multiple light-curve measurements spread over many orbital cycles can enable very high precision period determination. The key lies in being able to unambiguously line-up stable features observed in widely separated observations. This process of phase connection can only be achieved if one already has a well-constrained measurement of the period, and the spacing between observations is such that the phase error does not accumulate to the point that the absolute phase of known features becomes ambiguous. This approach has been widely used (throughout the history of astronomy) to determine the orbital periods of binary stars (e.g. Singh et al. 2002 in the case of Cyg X-3). With a sufficiently accurate period we can identify the orbital phase of the X-ray observations, and existing optical data points. Very high precision measurements of the orbital period are required in order to detect period derivatives in HMXBs; model predictions for IC 10 X-1 suggest $\Delta P/P \leq 10^{-6}$ (Tutukov et al. 2013).

In the case of the *Chandra*/*XMM–Newton* monitoring of IC 10 X-1, we have 12 observations (Table 1) one pair of which (07082, 08458) show unambiguous eclipse egress and ingress, respectively (Prestwich et al. 2007). The remaining 10 observations are randomly spaced, and so should contain a range of orbital phases. The final *XMM–Newton* observation is special because it covers a full orbital cycle and thus provides a chance to confirm the picture arrived at from the *Chandra* monitoring. It also greatly extends the baseline, such that a 1 s departure in the ephemeris becomes a $\Delta\phi = 2$ per cent phase shift over the 2500 orbital cycles encompassed by a decade. In order to interpret these data, we need to know the orbital phase of each one.

The orbital period of IC 10 X-1 was first determined from a dense week-long series of *Swift* X-ray observations by Prestwich et al. (2007), yielding $P = 34.40 \pm 0.83$ h (123840 ± 2988 s). Shortly thereafter an optical radial velocity study by Silverman & Filippenko (2008) using Keck produced a more precise ephemeris $P = 34.93 \pm 0.04$ h (125748 ± 144 s). Maintaining phase connectivity over many orbital cycles requires that the binary period be known to a corresponding level of precision. The published period has a precision of $\Delta P/P = 1.145 \times 10^{-3}$ (approx. 0.11 per cent). Accordingly the accumulating orbital phase error exceeds 10 per cent after 88 binary periods (128 d) have elapsed, and total loss of phase ($\Delta\Phi = 0.5$) occurs after 437 cycles, or 1.75 yr. The largest spacing between X-ray observations is ∼3 yr and the smallest is 2 d (see Table 1). Thus in principle phase connection can be achieved provided that recognizable features can be discerned in the light-curve segments.

We explored a set of trial periods centred on the published orbital period of Silverman & Filippenko (2008) and extending by ± 1 per cent on either side. Folded light curves were generated for
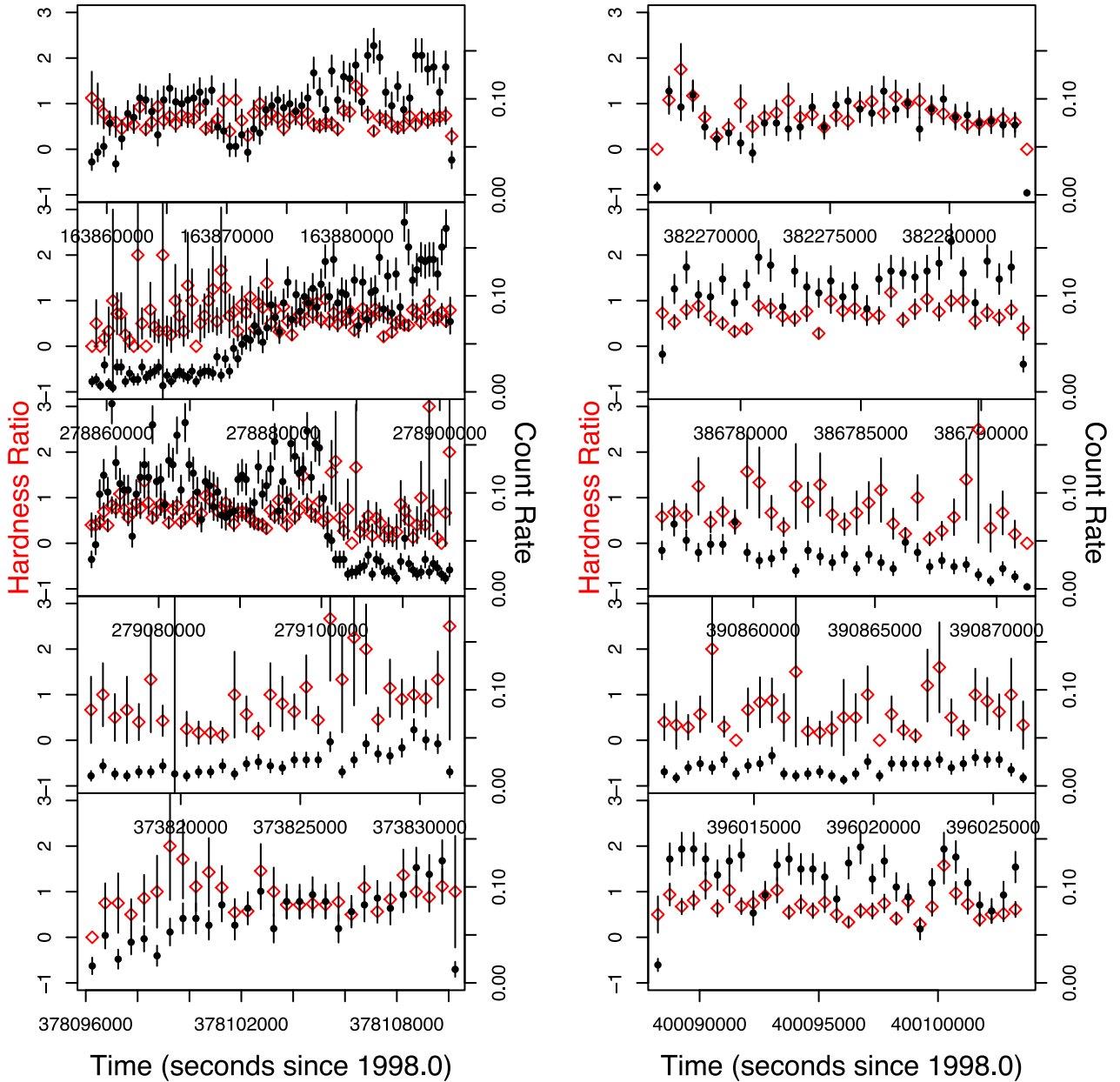
Figure 2. Light curves and HRs at 500 s resolution for all 10 *Chandra* observations. All plots share the same *Y*-axes: net CRs (corrected for exposure map) are plotted as solid dots, with scale on the right-hand *Y*-axis, HRs are red diamonds with scale on left *Y*-axis. The *X*-axes are chronological sections of the mission timeline (seconds since 1998.0 TT). The second and third panels (ObsIDs 07082 and 08458) contain, respectively, the clearest examples of eclipse egress and ingress.

1500 trial periods in 1 s increments to create a movie of the resulting phase-folded light curve. Visualized in this way it was possible to examine how the various light-curve segments fit together, and see the effects of changing the period and epoch. Naturally the more distant an observation is from the epoch, the more its phase moves in response to a very small change in period. Each event's arrival time was transformed to orbital phase using the *ObsID 07082* mid-eclipse time to define phase $\Phi = 0.5$, which set the folding zero-point or epoch ($T_0 = 278\,801\,348$ mission seconds = MJD 54040.87). To avoid negative phases we subtracted 100 000 cycles of the trial period from the actual time of mid-eclipse, as given in equation (1). The *XMM–Newton* data were included by folding the XSA pipeline light curve on the same ephemeris. The time sys-

tems used to tag *Chandra* and *XMM–Newton* data share the same reference point (elapsed seconds since 1998.0 TT) so no time conversion is required:

$$\Phi = \frac{(t - T_0 - 100\,000P)}{P}. \tag{1}$$

Once all of the events (or light-curve bins) are transformed to phase, they are grouped into histogram bins within each contiguous observation. This yields a set of 10 histograms, the binning scheme (breakpoints between bins) is chosen so that each data set is binned to an appropriate resolution given the number of events present and the duration of the observation. We tried a variety of algorithms including fixed width (0.1 or 0.05, and 0.02 in phase) and the Scott
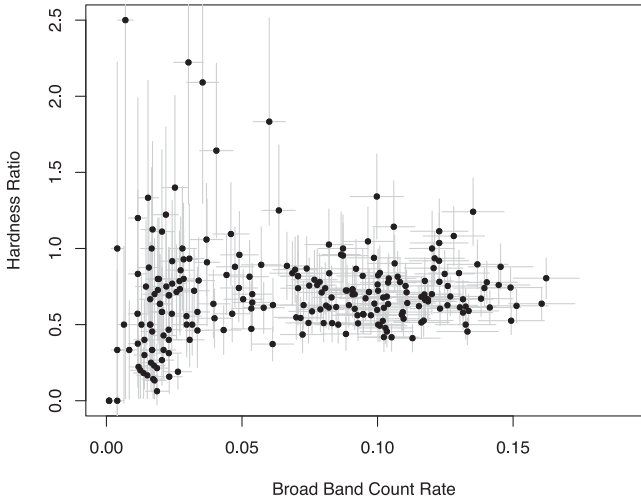
Figure 3. X-ray count rate versus HR diagram for the combined *Chandra* data. The net CR is in the broad 0.3–8 keV band, the HR is constructed from the ratio of hard band/soft band in 1000 s bins. There is a well-defined split between high and low flux values, occurring at CR = 0.06.
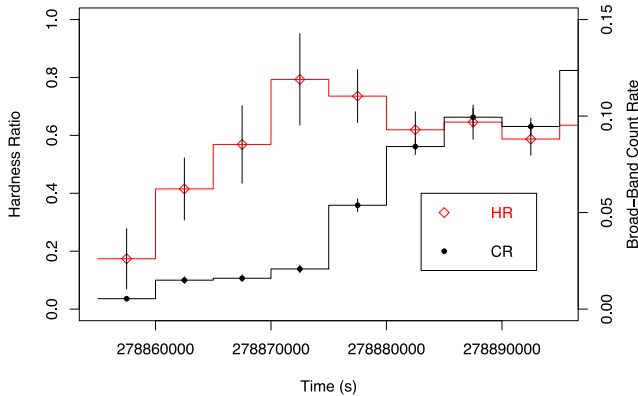

Figure 4. Plot of HR during the eclipse egress seen in observation 07082, binned at 5000 s intervals to reveal the steady rise in HR as the BH moves out of eclipse. The flux increase appears to lag the rise in HR. The midpoint of this eclipse occurred on MJD 54040.87, which defines the reference epoch used throughout this paper.

(1992) formula for optimal bin choice. A change of 1 s in the trial period represents a cumulative phase shift of 0.002 yr^{-1}, accumulating over a decade to 0.02. Consequently the smallest useful bin size is of order $P/100$ or so. The CR in each phase histogram bin is calculated as the number of events in the bin, divided by its width in seconds. The CRs for each observation are then divided by the normalized exposure map value for the extraction region in the original *Chandra* images. No correction is applied for extraction region size, since we used regions scaled to a fixed fraction of encircled energy [determined from the High Resolution Mirror Assembly (HRMA) point spread function (PSF) model]. The phase histogram of all 10 observations is plotted in different colours in Fig. 5 which appears in the online journal as an animation stepping through the range of trial periods; the figure shows a single frame at the 'best period'. As a comparison, we also folded a binned light curve (100 s time bins, and incorporating exposure map correction) for each trial ephemeris, and plotted the resulting points and their statistical error without re-binning by phase. This representation shows the intrinsic scatter in the flux values, and is shown in grey in Fig. 5.

Visual inspection showed no trial period places all low-flux observations in eclipse and simultaneously all high-flux observations outside of eclipse, leading to three possible scenarios: (1) either the X-ray source can sometimes become visible during eclipse (requiring it to become more spatially extended); (2) the system alternates between different states such that it can show low flux even when not eclipsed; (3) the true period lies slightly outside the reported range.

Applying the condition that no high-flux values should conflict with the eclipse profile defined by the near-contiguous observations (ObsIDs 07082, 08458), but allowing low-flux values to fall outside of the eclipse, we devised a numerical test to search for candidate periods. It was not possible to use other established methods (e.g. O − C) because most of our samples of the light curve contain no a priori recognizable features. At each trial period, we recorded the number of photon events falling inside the eclipse, expecting that the correct period will yield a minimum value. By treating the *Chandra* and *XMM–Newton* data separately we have two independent test statistics. We first define a reference eclipse and epoch, and set a nominal eclipse width as follows.

We chose the folding zero-point ($T_0 = 278\,801\,348s = $ MJD 54040.87) such that the midpoint of the *Chandra* 'reference eclipse' lies at phase 0.5 in our plots. The full width of the reference eclipse is 0.2 in phase, so the region $\Phi = 0.4$–0.6 should contain minimal flux for an acceptable binary period. At each trial period, we record (separately) the number of ACIS and *XMM–Newton*-PN counts falling inside the eclipse, and then plot the results in Fig. 6. Note that two slightly different versions of the *Chandra* statistic are plotted: one from the unbinned event times, and the other from the binned light curve (which includes exposure map correction). The value of these statistics only changes with period if the number of events falling within the selected eclipse range changes, so there are some flat regions in the graph. Fig. 6 reveals a series of local minima roughly evenly spaced in trial period–space. Each minimum is very narrow, and we can definitively exclude any trial period not lying in such a minimum. The resulting set of candidate periods can then be compared with other independent constraints in order to see if they intersect.

Within the 3σ period range reported by Silverman & Filippenko (2008), indicated in Fig. 6, we find eight minima in the *Chandra* statistic, and seven in the *XMM–Newton* statistic. Most of these minima are mutually exclusive between the *XMM–Newton* and *Chandra* series, leaving just four candidate periods. The minima have a regular spacing driven by the difference in period needed to accumulate phase shift in integer multiples of the orbital period for the various observations comprising the time series. Visual inspection of the corresponding folded light curves reveals that one of the candidate periods ($P = 125\,431$ s $= 1.45\,175$ d) places more of the low-flux observations inside eclipse, as shown in Fig. 5. The 'best' period simultaneously places the *XMM–Newton* observations of 2003 and 2012 right on top of the *Chandra* reference eclipse (2006) and reveals close consistency between the eclipse profiles in the two *XMM–Newton* observations. The rising portion of the 2003 observation is thus confirmed to be an eclipse egress, as its profile is an exact match to the 2012 egress within errors. Evidently the source luminosity and extent of the emission region are the same in both observations. Flaring of similar amplitude and duration is also seen at both epochs.

To estimate the uncertainty of the orbital period measurement, we again consider the accumulating phase drift across the entire data set. Relative to the vertical lines at $\phi = 0.4$, 0.6 plotted in Fig. 5 neighbouring trial periods at ± 1 s cause features to shift by
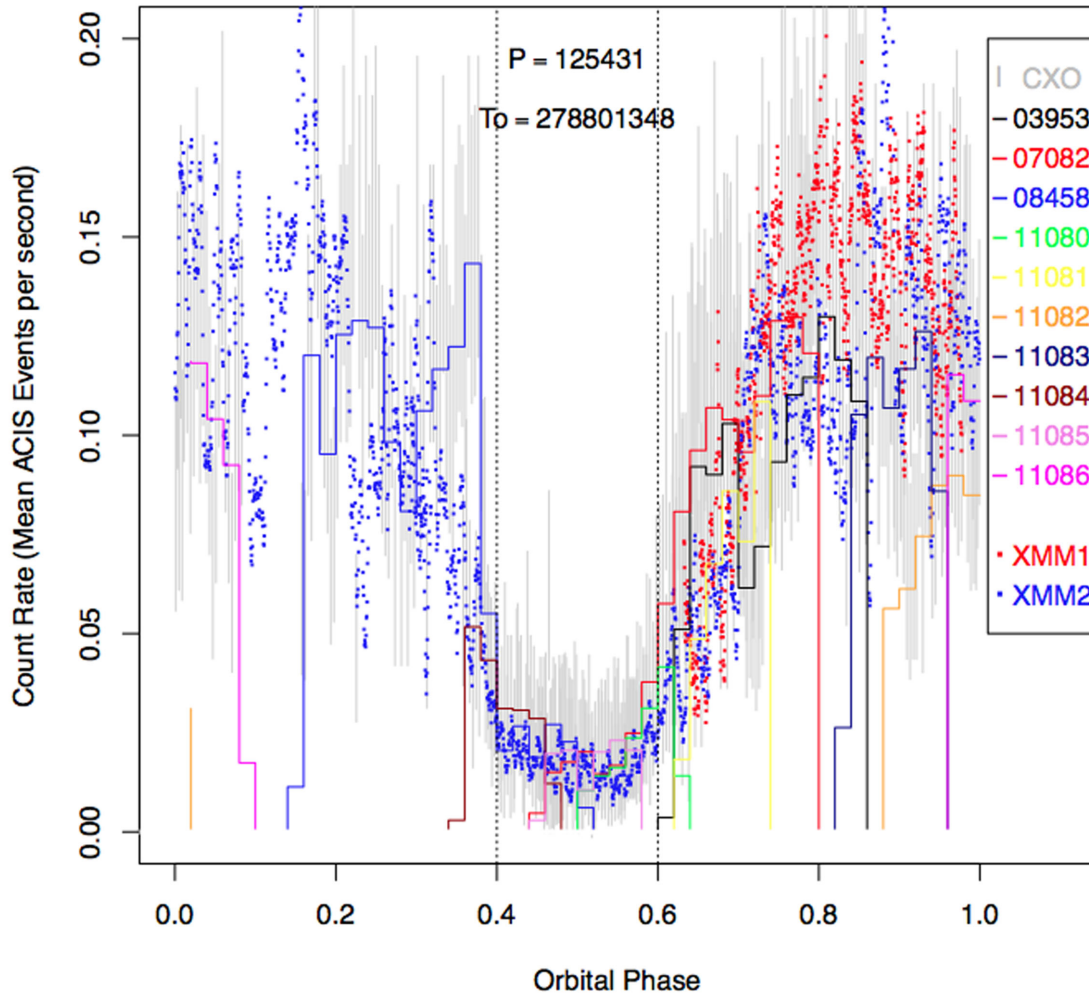
Figure 5. Phase-folded light curve for all 10 *Chandra* and two *XMM–Newton* observations, for a trial period of $P = 125\,431$ s (1.45175 d), based on visual inspection and eclipse–flux analysis of the light curves produced by a range of trial periods spanning 1 per cent either side of the published orbital period. This period lies within 2σ of the published value from the optical RV study of Silverman & Filippenko (2008). An animation of the folded light-curve segments stepping through 1500 trial periods is available in the online journal.

$\Delta\phi = 0.02$ such that a drift of 2 s in either direction causes the eclipse feature to unravel.

As a further check on our candidate period, we computed a Lomb–Scargle periodogram (LSP) for the entire *Chandra* light curve binned at 100 s resolution. For *Chandra* data alone the resulting highest peak is at $P = 125\,439$ s. We then recomputed the LSP for the combined *XMM–Newton* and *Chandra* time series which is plotted in Fig. 7, obtaining $P = 125\,435$ s (half-width at half-maximum = 20 s). To assess significance, uncertainty and the influence of the observing cadence we ran a 1000 iteration Monte Carlo, randomizing the light-curve points among the actual observation times and re-computing the LSP. We find all features in Fig. 7 lie far above the power distribution for uncorrelated light curve; the observed pattern in the LSP is therefore due to aliasing. We performed a second Monte Carlo involving the addition of a periodic component matched to the observed modulation (period = 125 435 s, amplitude = 0.05 counts s^{-1}) to the randomized flux values. The phase of the simulated periodicity was changed at random for each trial. The recovered periods ranged between 125 432 and 125 438 with a standard deviation of 1.1 s. A similar pattern of alias peaks occurred in all trials and never exceeded the power at the

true period. The eclipse folding analysis and the LSP are therefore consistent, having different systematic errors.

5 ANALYSIS OF THE X-RAY ECLIPSE PROFILE

For a point-like X-ray source and a primary star with a clearly delineated boundary, a total eclipse should appear as a nearly rectangular dip. The duration of the minimum gives the diameter of the larger star, and the duration of the ingress or egress gives the diameter of the X-ray emission region. In reality more complex morphology results from X-ray scattering in the wind of the companion, the existence of extended emission and absorption components (e.g. accretion disc, corona, impact hotspot), partial eclipses, and gravitational distortion of the companion (Orosz et al. 2007). The following processes can in principle blur the edges of the eclipse. (a) In the typical low CR regime the binning process needed to visualize the light curve will automatically impose a loss of timing resolution. (b) The X-ray source may indeed be extended (in this context extended means its diameter is larger than the product of the timing resolution and the relative velocity between the two stars.). (c) The column density
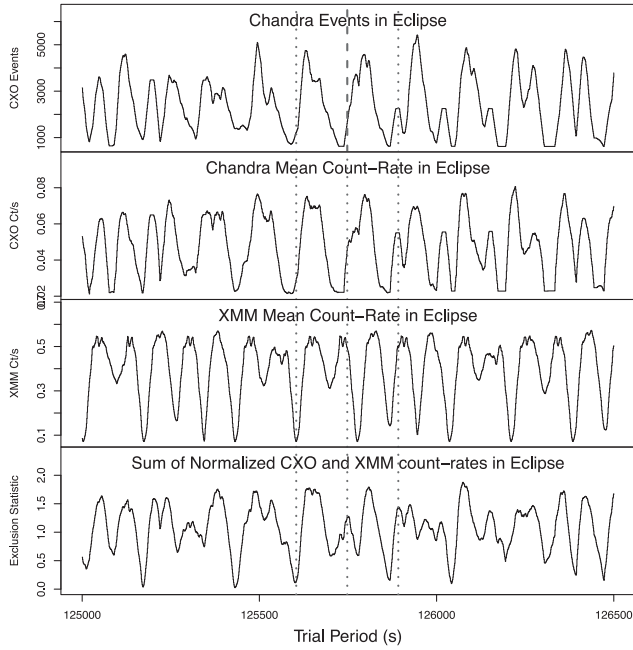
Figure 6. Eclipse periodograms created by the *Chandra* and *XMM–Newton* events and CR inside the reference eclipse (phase = 0.4–0.6) for trial periods spanning 1 per cent either side of the established orbital period. Vertical dotted lines indicate the Silverman & Filippenko (2008) period and its 1σ uncertainty. Minima correspond to trial periods that produce a consistent ephemeris. The *Chandra* and *XMM–Newton* data each define an independent set of minima. The bottom panel shows the intersection of these sets, resulting in a smaller set of mutually consistent periods.
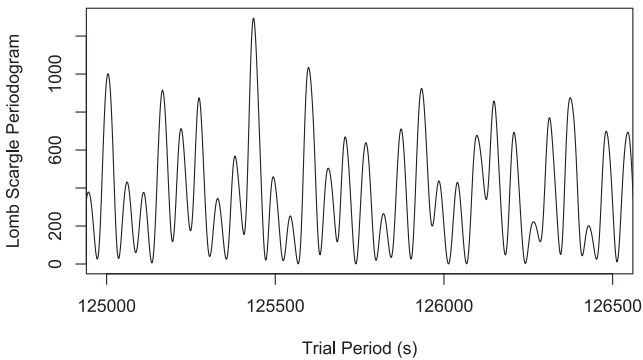

Figure 7. Lomb–Scargle periodogram for the combined *Chandra*+*XMM–Newton* light curve. The highest peak is at a period of 125 435 s or 34.84306 h. Monte Carlo simulations reveal that the pattern of additional peaks is consistent with aliasing. (The 99.9 per cent significance level is 8 for an uncorrelated light curve.)

of stellar wind particles increases rapidly as the BH approaches first contact so increasing absorption could blur the otherwise sharp cut-off. (d) Reprocessed X-rays scattering through the wind of the primary star could continue to be seen after the X-ray source passes second contact. (e) Finally, intrinsic X-ray variability is convolved with the underlying eclipse profile.

The eclipse profile seen in the *Chandra* data (Fig. 5) is deep and well defined. The duration of minimum flux is approximately 5 h (0.15 in phase), during which the background subtracted CR never reaches zero, remaining above the rate observed in the diffuse emission surrounding the point source. The full width of the X-ray eclipse is about 7 h $\Phi = 0.2 \pm 0.05$. The region is marked in Fig. 5
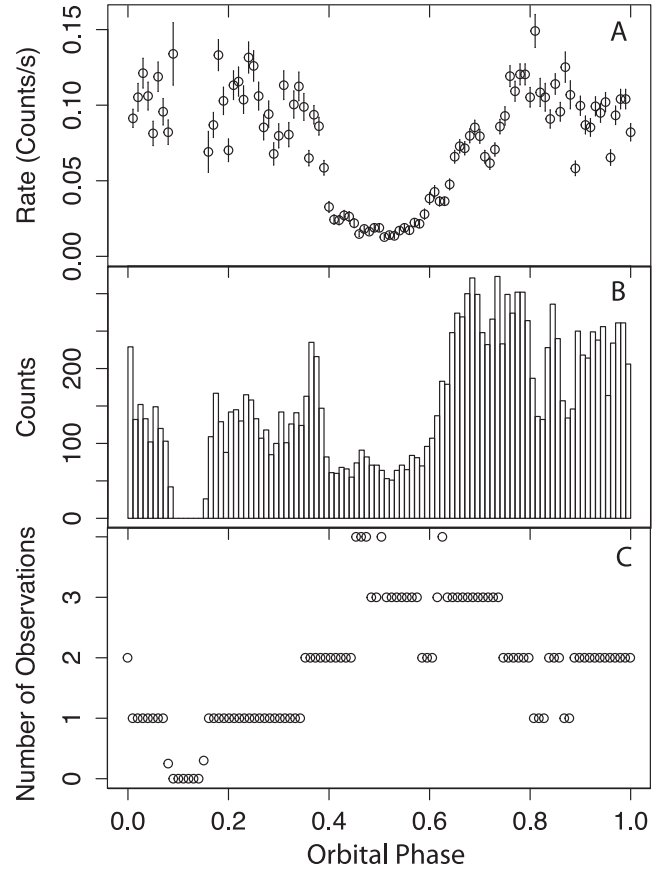

Figure 8. The average *Chandra* eclipse profile (A) was computed by dividing the total number of counts in each phase bin (B) by the number of observations at each phase bin (C) to effect a correction for fractional exposure.

by vertical dotted lines. To study the shape further we generated an average eclipse profile from the entire *Chandra* data set to improve S/N, and correct for fractional exposure. The resulting average 0.3–8 keV profile is shown in panel (A) of Fig. 8. The raw folded/binned light curve and the number of observations contributing to each phase bin are shown in panels (B) and (C), respectively.

The *Chandra* eclipse profile shows an asymmetry between the ingress and egress. The flux undergoes a very steep drop from phase 0.38 to 0.42, remains at minimum until phase 0.6 and then climbs steadily until phase 0.7. Many other accreting binaries (HMXBs, LMXBs, and cataclysmic variables, CVs) show a comparable asymmetric eclipse shape which is regarded as the signature of an accretion disc hotspot. As the compact object moves into eclipse it is partly obscured by matter streaming on to the accretion disc, because of angular momentum conservation this hotspot trails the BH in its orbit, when the BH re-emerges it leads the hotspot, emerging clear of the accretion stream while the hotspot is still hidden, leading to a deficit in intensity at egress (see e.g. Rutten, van Paradijs & Tinbergen 1992). We also see higher levels of variability before ingress than at other times, similar to the BH–HMXB M33 X-7 (Pietsch et al. 2006; Orosz et al. 2007).

The eclipse exhibits ingress and egress stages of duration $\phi \sim$ 0.05, indicating a length-scale of 1.5–$2\,R_\odot$ for scattering and/or extended emission. There are several independent observations of eclipse egress (two from *XMM–Newton* and panel C of Fig. 8 shows the coverage by *Chandra*), all show a feature at phase 0.7. Either it is a dip centred at phase 0.7, or a brightening just prior which ends

at phase 0.7. This feature is evident in binned average light curve shown in panel (A) of Fig. 8 constructed from all the *Chandra* data. If it truly is stable, then it could be due to the emergence of the trailing side of the accretion-disc with its attendant hotspot.

The eclipse is broader and more gradual in the *XMM–Newton* data than in the *Chandra* data. We attribute this to energy dependence of the eclipse profile originating from absorption and scattering by the stellar wind. *XMM–Newton* has a greater effective area at low energies resulting in it seeing a broader eclipse.

5.1 Calculating the binary parameters and the size of the X-ray shadow

Following the usual procedure for determining the dimensions of an eclipsing binary system (e.g. Charles & Seward 1999; Carroll & Ostlie 2006) we assume circular orbits and inclination $i = 90°$, and make use of the following results from Clark & Crowther (2004), Prestwich et al. (2007), and Silverman & Filippenko (2008): The RV semi-amplitude of the WR star is 370 ± 20 km s^{-1}; the mass of the WR is most likely $35\,M_\odot$, requiring the mass of the BH to be $32 \pm 2.6\,M_\odot$. The lowest acceptable mass for the system has $M_{WR} = 17$ and $M_{BH} = 23.1 \pm 2.1\,M_\odot$. In the former case the WR star is the most massive member of the binary, and in the latter the BH is the more massive. These alternative scenarios are summarized in the first four lines of Table A1 of Appendix A. We estimate the duration of minimum X-ray flux in Fig. 5 to be 5 h, with ingress/egress each lasting about 1 h.

For circular orbits, the following relations follow from Newtonian mechanics: $m_1/m_2 = v_2/v_1 = a_2/a_1$ and in addition the tangential velocities (v_1, v_2) and separations (a_1, a_2) are constant and are related via Kepler's third law.

If the orbital plane lies along the line of sight (which it must be close to since the system has deep eclipses), then the relative velocity between the two stars is $v_{rel} = v_1 + v_2$, and as seen from the Earth this is equal to the distance travelled by the BH relative to the WR star divided by the eclipse duration ($v_{rel} = 2R_{WR}/T_{eclipse}$). Hence the measurement of the eclipse duration yields $R_{WR}\sin(i) = T_{eclipse}(v_1 + v_2)/2$.

Using these relations, we calculate the range of radii corresponding to the 'most massive' and 'least massive' cases to be $R_{WR}^{max} = 10.1\,R_\odot$ and $R_{WR}^{min} = 8.4\,R_\odot$. The respective orbital separations are $(a_1 + a_2)\sin(i)^{max} = 1.527 \times 10^{10}$ m ($21.923\,R_\odot$) and $(a_1 + a_2)\sin(i)^{min} = 1.286 \times 10^{10}$ m ($18.46\,R_\odot$). The inferred separation depends weakly on the masses and inclination (given the observational constraints on the mass function and inclination). The results are given in Table A1 and compared to the same calculations for other known BH-HMXBs as discussed in Section 8. The corresponding estimates for the length-scale of the wind-scattering region and/or extended X-ray emission (as inferred from the duration of ingress/egress portions of the light curve) are 2.0 and 1.7 $R_\odot$.

We performed identical calculations for the other known BH-HMXBs and summarize the results (and citations) for reference in Appendix A and Table A1. We notice that the other WR systems (NGC 300 X-1, Cyg X-3, and the object in NGC 4490) show similarly broad X-ray modulation (Belczynski et al. 2013). Of these only NGC 300 X-1 is known to be eclipsing, and our calculation shows that it too has eclipse shadows of order 10 $R_\odot$. In contrast the supergiant (SG) system M33 X-7 has an eclipse duration in good agreement with its stellar radius as inferred from other means, as is typically seen in eclipsing neutron star+SG HMXBs.

With these approximate dimensions we can estimate the possible range of inclination angles for the system such that a point-like BH

undergoes total eclipses (while the extended or scattered emission could remain visible). The angular radius of the star (or its dense wind) as seen from the BH is $\sin(\theta) \sim R/(a_1 + a_2)$. For the radii calculated above, this results in $\theta = 27°$ for either scenario (both the separation and stellar radius increase with mass). The minimum inclination angle for eclipses is then $i = 90 - \theta$, which gives $i > 63°$. We also calculated the RV semi-amplitude that would result for different values of the inclination, while keeping P_{orbit} fixed and remaining within the allowed range of masses. We found that RV_{max} remains below the maximum possible 390 km s^{-1} (RV+error) for $i > 71°$. For the WR star itself to eclipse the BH the limiting inclination is $i < 85°$.

6 COMPARISON BETWEEN X-RAY AND OPTICAL RADIAL VELOCITY OBSERVATIONS

As a direct comparison between our X-ray eclipse ephemeris and existing optical spectroscopy, we analysed the published He II [λλ4686] line RV data of Silverman & Filippenko (2008). We used a similar procedure to the one described in Section 4 to test trial periods against the reference eclipse. At each trial period we transformed the optical observation times (published as HJD and converted to seconds since 1998.0 using XTIME[5]) to X-ray eclipse phase (where 0.5 is defined as mid-eclipse as in equation 1 and Figs 5 and 8) and then fit the RV data with an antisinewave of amplitude 370 km s^{-1}. The only free parameter in the fit is a phase shift. The value of the phase shift quantifies agreement between the RV data and the X-ray ephemeris. Our method tests the assumption that the mid-point of the reference eclipse corresponds to inferior conjunction (the point in the orbit when the WR star switches from moving towards us and begins moving away). The resulting array of phase shifts is plotted against trial period in Fig. 9 revealing just three trial periods (125 077, 125 551, and 126 031 s) that satisfy this criterion. The phase shift between the X-ray and optical observations should be consistent with zero if the He II line originates on the WR star, while values close to ±0.5 would place the emission close to the BH. Of the three periods thus identified only $P = 126\,031$ falls in a minimum of the X-ray eclipse periodograms plotted in Fig. 6, both of the others being ruled out. The lone surviving period does not give the deepest eclipse minimum, and is not the period identified in the LSP. Examination of the eclipse-folding animation (accompanying online data for Fig. 5) shows this period is problematic as it places all of the low-flux *Chandra* observations far outside eclipse.

Our preferred X-ray period of 125 431 s (1.45175 d) produces a phase shift of -0.25 ($-\pi/2$ rad) which *either* places the He II emitting material trailing the WR star around its orbit by up to $90°$ or implies that the eclipse occurs substantially before inferior conjunction. If the He II line originates in the wind, it raises the question of the origin of its asymmetry with respect to the star. Photoionization of the wind by X-rays will restrict the physical conditions for line emission to regions shadowed by the star and regions sheltered by sufficiently high column density of wind particles. Depending on the exact geometry, the observed RV curve will involve contributions from orbital motion, wind velocity, and rotational velocity of the star.

An appealing mechanism exists for producing an asymmetric density structure in the binary system, which naturally results in eclipses that precede inferior conjunction. Persistent spiral shock structures known as pinwheels or dust spirals form in the winds of
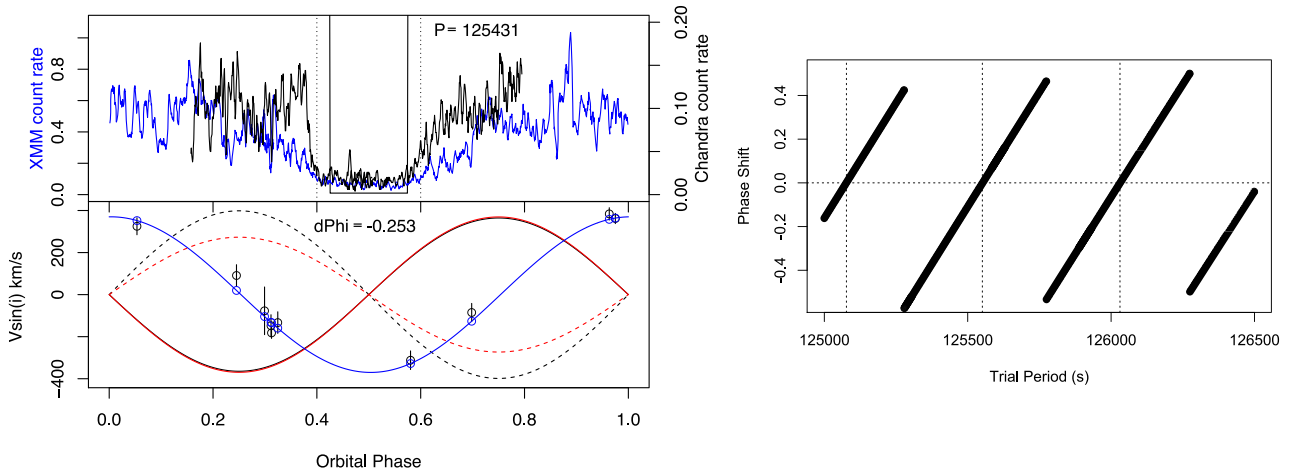
---

[5] http://heasarc.gsfc.nasa.gov/cgi-bin/Tools/xTime/xTime.pl

Figure 9. Comparison of X-ray eclipse ephemeris with optical radial velocity data. Left-hand panel: reference eclipse (top) and RV curves (bottom) using the ephemeris ($P = 125\,431$ s or 1.45 175 d, $T_0 = $ MJD 54040.87) and assuming $i = 90$. The solid red line is the model curve for the WR star, whose motion changes sign from approaching to receding (i.e. inferior conjunction) at the midpoint of the reference eclipse. Dashed lines are the model RV curves for the BH that would result for the two mass scenarios considered in the text. Points with error bars are the published He II RV values of Silverman & Filippenko (2008) folded on our ephemeris. Solid blue curve is the best-fitting sine wave to the RV points, used to determine the phase shift between the RV points and the model. Right-hand panel: the phase shifts resulting from repeating this analysis over a range of trial orbital periods. Dotted lines indicate the specific trial periods for which the RV derived inferior conjunction occurs at phase = 0.5.

close binaries containing WR stars. The prototype colliding-wind pinwheel is WR 104 (Tuthill et al. 2008; Monnier et al. 2011) consisting of a WR+OB in a 241.5 d orbit. The high-velocity wind of the WR collides with the weaker wind of the secondary forming a shock front. Behind this front the WR wind stalls, pushing up its density and allowing dust grains to form. In the case of WR 104 the region of elevated density trails behind the O-star while moving outwards, tracing out a spiral. If the same physics occurs in IC 10 X-1, then the dense region is trailing behind the BH and will lie between the observer and the BH when the BH is moving directly away from us (and hence the WR moving directly towards us). The deepest part of the X-ray eclipse should coincide with the time of maximum blueshift of the He II line. This situation is what we see in Fig. 9. If this interpretation is correct the size of the dense region can be approximately inferred from the eclipse duration and the circular orbital velocity of the BH (see Table A1), resulting in 5–7 × 10^6 km. Equivalently during the ~5 h eclipse, the BH moves through 5/35 of its orbit. The wind velocity encountered by the BH will be lower in IC 10 X-1 than in WR 104 due to the smaller orbital separation. The orbital (and angular) velocities however are much higher, consequently rotation-induced effects need to be incorporated into any model. The phase shift can also relieve the geometric constraint on the orbital inclination. If X-ray eclipse does not correspond to inferior conjunction, then the WR star is not actually eclipsing the BH, and the X-ray modulation could be entirely due to absorption and scattering in the wind.

7 SPECTRAL CHANGES

ACIS-S pulse-height spectra with sufficient counts for spectral analysis are available for all 10 *Chandra* observations (Table 1). Using the 2003 ACIS-S data Bauer & Brandt (2004) found that the point source is embedded in spatially extended X-ray emission, and described a two-component spectral model consisting of a power law ($\Gamma = 1.8$) plus a thermal plasma ($kT = 1.5$ keV), accompanied by an absorbing column consistent with IC 10 ($N_H = 6 \times 10^{21}$ cm^{-2}). The power-law component dominates the point-source spectrum,
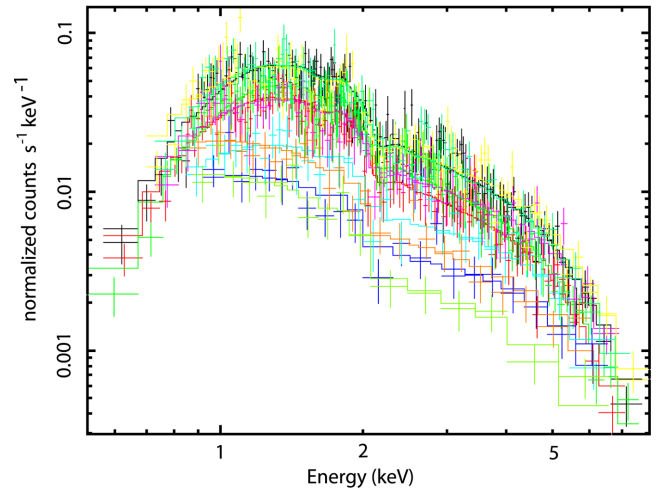

Figure 10. *Chandra* X-ray spectra of the 10 observations in Table 1. Each spectrum is fit by an absorbed power law, the parameters are given in Table 2 (the spectra can be identified from their flux).

and the thermal component appears to be associated with the extended emission. Wang et al. (2005) found the 2003 *XMM–Newton* PN+MOS spectrum (which has higher S/N) is more consistent with a Comptonized multicolour disc blackbody (MCD) with inner temperature $T_{in} = 1.1$ keV, and that the *Chandra* data are well described by the same model. The parameters of the MCD model are such that a high value of the BH's spin is required in order to reconcile the spectral fit with the large mass implied by the mass function. Residual structures reported by Bauer & Brandt (2004) as evidence of photoionization lines were interpreted by Wang et al. (2005) as artefacts of the data reduction which was complicated by pile-up correction and the presence of background flares.

In order to search for spectral variations the 10 ACIS-S pulse-height spectra are plotted on the same axes in Fig. 10, and the results of the spectral fitting to each observation are given in Table 2. For

Table 2. X-ray spectral parameters for IC 10 X-1.

ObsID	N_H (10^{21} cm^{-2})	Γ	Norm ($\times 10^{-5}$)	Flux	χ^2/dof
03953	5.4 ± 0.3	1.81 ± 0.07	38.5 ± 2.85	1.34	151/155
07082	4.3 ± 0.3	1.77 ± 0.07	30.8 ± 2.33	1.087	152/136
08458	5.5 ± 0.3	1.90 ± 0.06	44.0 ± 3.13	1.29	198/155
11080	5.0*	1.41 ± 0.13	7.00 ± 0.82	0.36	34/22
11081	5.0*	1.48 ± 0.10	20.7 ± 1.91	1.10	36/34
11082	2.8 ± 0.6	1.31 ± 0.11	15.9 ± 2.18		67/66
11082*	5.0*	1.58 ± 0.07	21.8 ± 1.36	1.02	77/66
11083	3.0 ± 0.5	1.48 ± 0.09	31.0 ± 3.25		103/87
11083*	5.0*	1.73 ± 0.05	42.0 ± 1.94	1.66	116/87
11084	5.0*	1.90 ± 0.11	13.5 ± 1.21	0.429	39/28
11085	5.0*	2.03 ± 0.16	8.61 ± 1.01	0.242	23/17
11086	4.3 ± 0.5	1.73 ± 0.10	42.0 ± 4.76	1.425	91/83

Notes. Starred entries denote a frozen parameter. Both free and frozen fits are reported for 11082 and 11083. Flux in units of erg cm^{-2} s^{-1} in the 0.3–8 keV band.

consistency (in the face of varying S/N) we used the simple absorbed power-law model. Our fitted model parameters for ObsID 03953 are consistent with those found by Bauer & Brandt (2004) for the same observation, although we did not include the thermal component, and made no correction for pile-up (which is mild at these CRs). Among observations there are no clear trends in spectral index with flux, although the index varies between 1.3 and 2.0 a change of 3.5σ (see Table 2).

We also grouped the seven 2009 spectra into low flux (11080, 11084, 11085) and high flux (11082, 11083, 11086) subsets. We performed simultaneous fits on the members of each subset, however, this yielded indistinguishable results for absorption and spectral index parameters ($N_H = 0.5, \Gamma = 1.5$), with poor fits in both subsets ($\chi^2 > 2.3$).

The variation in spectral index (Table 2) mirrors the HR behaviour seen in Fig. 1, confirming the picture of an event lasting perhaps weeks–months, beginning some time before 2009 November, and concluding during the monitoring series in early 2010.

8 CONCLUSIONS

We have used *Chandra* and *XMM–Newton* observations spanning 2003–2012 to study the light curve and spectral changes in the BH X-ray binary IC 10 X-1. These observations provided information on the long-term stability of the X-ray emission, and enabled the eclipse duration to be measured. The X-ray eclipse minimum lasts for 5 h, which combined with the previously reported mass function, leads to a larger than expected radius for the X-ray shadow cast by the stellar companion. X-1's luminosity is typically 7×10^{37} erg s^{-1} outside of eclipse, but during 2009 exhibited an interval of slightly lower luminosity coinciding with a hardening of the spectrum.

The eclipse features in the long-term X-ray light curve were used to phase connect the entire data set leading to a refinement of the orbital period. Only a small number (4) of distinct candidate orbital periods are able to consistently and simultaneously fold the *Chandra*, *XMM–Newton*, and optical RV data. The most consistent X-ray period is 1.45175(1) d, which is the *only* such period that places all low-flux values inside eclipse, *and* all high-flux values outside of eclipse. Continued X-ray monitoring to capture additional eclipses will break the degeneracy between the candidate binary periods identified in this study. The ephemeris will then be known to an accuracy of $\frac{\delta P}{P} < 8 \times 10^{-6}$, enabling subsequent measurement of

its period derivative; for example by follow-up optical RV measurements to track the accumulating phase shift.

Orbital period derivatives have now been measured for several BH-HMXBs including XTE J1118+480 ($\dot{P} = -1.90 \pm 0.57$ ms yr^{-1}), A0620-00 ($\dot{P} = -0.60 \pm 0.08$ ms yr^{-1}) (González Hernández et al. 2014), and Cyg X-3 ($\frac{\dot{P}}{P} = 1.2$–4×10^{-6} s^{-1}; Lommen et al. 2005). Simulations by Tutukov et al. (2013) predict $\frac{\dot{P}}{P} = 5.8 \times 10^{-6}$ s^{-1} for IC 10 X-1. Based on the mass loss expected for the WR companion, IC 10 X-1's accretion rate and hence X-ray luminosity should be $\frac{1}{2}$ Eddington, which is an order of magnitude higher than what is observed. They were able to reconcile the observed L_X with the generally assumed mass of the system only by making the mass-loss rate lower. Since accreted matter transfers orbital angular momentum the rate of increase of the binary period scales with $\dot{M}$ and hence with the wind properties.

It is thought (see e.g. Prestwich et al. 2007) that the mass-donor star in IC 10 X-1 has a radius in accordance with the tabulated parameters of WR stars (Langer 1989), which would be 1.7–2 R$_\odot$ for the most massive case and 1.3–1.5 R$_\odot$ for the minimum mass case. The measured RV amplitude of 370 km s^{-1} (Silverman & Filippenko 2008) combined with this size estimate leads to a prediction of eclipse durations of approximately an hour in either of the mass ratio scenarios considered (Table A1). There is a (factor of 5) discrepancy between that prediction and the eclipse profile in Fig. 5 showing the X-ray shadow to be much larger than can be accounted for by the star alone. Further refinements to the orbital model will not reduce the radius value significantly, since the corrections will mostly go in the other direction. For example if the eclipse is partial due to a lower inclination, then the chord length traversed during eclipse becomes a smaller fraction of the stellar diameter, requiring the star to be bigger. Similarly the projected velocity would be a smaller fraction of the orbital velocity, requiring the star to be larger and also more massive. Although we have ignored tidal distortion of the companion, the effect is again to underestimate the size of the star, since we only measured the projected radius in its shortest orientation. The initial radii of the progenitor stars were certainly much larger than the 1.5–2 R$_\odot$ typical of WR stars. de Mink et al. (2010) show that the progenitors of BH–HMXB systems were larger than the present-day binary separations. As a comparison Allen (2000) gives the radius of a 35 M$_\odot$, O SG as 19 R$_\odot$, which is close to the orbital separation we measured for X1.

Compton scattering and absorption in the wind of the secondary are expected to be significant factors in shaping the eclipse profile, given the mass-loss rate is 10^{-6}–10^{-5} M$_\odot$ yr^{-1}. In the O-star binary M33 X-7, passage of the BH through the dense wind at ingress/egress extends the eclipse by $\sim$10 per cent due to absorption and scattering (Orosz et al. 2007). In comparison for IC 10 X-1 the WR star's wind being much denser will lead to a stronger scattering/opacity feature, as observed here.

A very broad X-ray modulation is also seen in LMC X-1 (which is not thought to be an eclipsing system) where the flux variation is energy independent suggesting electron scattering as the dominant opacity mechanism (Orosz et al. 2009). By comparison the density and velocity of the wind in IC 10 X-1 are poorly constrained, as is the degree of wind ionization, which was taken to be totally ionized in LMC X-1. The HR behaviour seen for IC 10 X-1 in Fig. 4 and the steeper/narrower eclipse seen by *Chandra* versus *XMM–Newton* both indicate the eclipse light curve is strongly energy dependent. However the general approach explains the extended duration of the eclipses in terms of wind scattering. An extended hard corona and the presence of neutral hydrogen in the eclipsing material can both produce an energy-dependent eclipse edge.

An intriguing possibility is that the steep edges seen in the *Chandra* eclipse profile for IC 10 X-1 mark the X-ray shadow of a shock or other density enhancements in the WR star's wind. WR winds are known to be highly asymmetric, although their termination shocks lie at ~1 pc (Eldridge 2007).

The optical RV measurements made of the He II line by Silverman & Filippenko (2008) present a complex picture when combined with the X-ray eclipse ephemeris. Three trial periods are able to place RV inferior conjunction at the mid-point of the reference X-ray eclipse. However, none of these periods is able to acceptably phase connect the X-ray data set. Conversely the acceptable X-ray eclipse derived periods all require substantial phase shifts between the epoch of mid eclipse and inferior conjunction. This eventuality was anticipated by Tutukov et al. (2013) and points to the need for additional spectroscopic observations to confirm the true origin of the He II emission and probe the structure of the eclipsing body. In Section 6 we presented a novel physical mechanism for the phase shift, invoking the dust pinwheel model of Monnier et al. (2011). A shock front must form where the WR wind collides with the wind from the BH accretion disc(Dotan & Shaviv 2011). Consequently a density enhanced region should trail the BH in its orbit and obscure the X-ray source when it passes in front, at 0.25 in phase before inferior conjunction. Recent hydrodynamic modelling of the WR+BH system Cyg X-3 by Okazaki & Russell (2014) shows that a dense wake probably trails the BH in its orbit, and is responsible for significant scattering and obscuration induced modulation of the X-ray source. This picture is markedly similar to the one we developed in Section 6.

The alternative (and more likely) interpretation is that the He II line does not directly trace the motion of the WR star, and instead originates in neutral (or partially ionized) gas shielded by a persistent structure in the stellar wind. It could be that the X-rays effectively fully ionize most of the wind as in LMC X-1 (Orosz et al. 2009), except for regions in the shadow of the star or wind density structures (of the type discussed above). The HR feature in the eclipses points to this being true. Emission lines require the gas to have a significant neutral content while being sufficiently energized to populate higher excited states in the atoms. Such a state of partial ionization for helium can exist above the temperature at which all hydrogen is destroyed, thus full shadowing is not required. Recombination will occur at large distances from the BH, and also in regions of enhanced wind density. The hypothesis could be tested by looking for the spectral lines emitted by other atomic and ionized species. The zone of partial ionization does not appear to be on the face of the star opposite the BH, although the orbital motion will be modified by the wind velocity, and perhaps also by stellar rotation.

Independent of which model is correct, the RV curve and X-ray eclipse are phase shifted, and interaction between the stellar wind and the BH's wind and radiation field are required to explain the offset.

Further X-ray (eclipse timing) and optical observations (RV and ellipsoidal modulation) are required in order answer key remaining questions about IC 10 X1, which is of fundamental importance for the study of both stellar and intermediate-mass BHs.

REFERENCES

Allen C. W., 2000, Allen's Astrophysical Quantities, 4th edn. Springer-Verlag, New York
Bauer F. E., Brandt W. N., 2004, ApJ, 601, L67
Belczynski K., Bulik T., Mandel I., Sathyaprakash B. S., Zdziarski A. A., Mikołajewska J., 2013, ApJ, 764, 96
Binder B., Williams B. F., Eracleous M., Garcia M. R., Anderson S. F., Gaetz T. J., 2011, ApJ, 742, 128
Bogomazov A. I., 2014, Astron. Rep., 58, 126
Bolton C.T., 1972, Nature, 102, 124
Carpano S., Pollock A. M. T., Prestwich A., Crowther P., Wilms J., Yungelson L., Ehle M., 2007, A&A, 466, L17
Carroll B., Ostlie D. A., 2006, Introduction to Modern Astrophysics and Cosmology, 2nd edn. Pearson, San Francisco
Charles P. A., Seward F. D., 1999, Exploring the X-ray Universe. Cambridge Univ. Press, Cambridge
Clark J. S., Crowther P. A., 2004, A&A, 414, L45
Crowther P. A., Barnard R., Carpano S., Clark J. S., Dhillon V. S., Pollock A. M. T., 2010, MNRAS, 403, L41
de Mink S. E., Cantiello M., Langer N., Pols O. R., Yoon S.-Ch., 2010, in Prša A., Zejda M., eds, ASP Conf. Ser. Vol. 435, Binaries – Key to Comprehension of the Universe. Astron. Soc. Pac., San Francisco, p. 179
Dotan C., Shaviv N. J., 2011, MNRAS, 413, 1623
Eldridge J. J., 2007, MNRAS, 377, L29
Esposito P., Israel G. L., Sidoli L., Mapelli M., Zampieri L., Motta S. E., 2013, MNRAS, 436, 3380
Frolov V. P., Zelnikov A., 2011, Introduction to Black Hole Physics. Oxford Univ. Press, Oxford
González Hernández J. I., Rebolo R., Casares J., 2014, MNRAS, 438, L21
Grinberg V. et al., 2014, A&A, 565, A1
Hanson M. M., Still M. D., Fender R. P., 2000, ApJ, 541, 308
Hutchings J. B., Crampton D., Glaspey J., Walker G. A. H., 1973, ApJ, 182, 549
Johannsen T., 2009, A&A, 507, 617
Langer N., 1989, A&A, 210, 93
Laycock S., Cappallo R., 2014, ApJ, 789, 64
Laycock S., Camero A., Wilson-Hodge C. A., Williams B. F., Corbet R. H. D., Marshall F. E., Galache J. L., Garcia M. R., 2010, BAAS, 42, #419.04
Lommen D., Yungelson L., van den Heuvel E., Nelemans G., Portegies Zwart S., 2005, A&A, 443, 231
Monnier J. D. et al., 2011, ApJ, 742, L1
Nowak M. A., Wilms J., Heindl W. A., Pottschmidt K., Dove J. B., Begelman M. C., 2001, MNRAS, 320, 316
Okazaki A. T., Russell C. M. P., 2014, in Ishida M., Petre R., Mitsuda K., eds, Suzaku-MAXI 2014: Expanding the Frontiers of the X-ray Universe. p. 202 (arXiv:1405.4808)
Orosz J. A. et al., 2007, Nature, 449, 872
Orosz J. A. et al., 2009, ApJ, 697, 573
Orosz J. A., McClintock J. E., Aufdenberg J. P., Remillard R. A., Reid M. J., Narayan R., Gou L., 2011, ApJ, 742, 84
Orosz J. A., Steiner J. F., McClintock J. E., Buxton M. M., Bailyn C. D., Steeghs D., Guberman A., Torres M. A. P., 2014, ApJ, 794, 154
Pasham D. R., Strohmayer T. E., Mushotzky R. F., 2013, ApJ, 771, L44
Pietsch W., Haberl F., Sasaki M., Gaetz T. J., Plucinsky P. P., Ghavamian P., Long K. S., Pannuti T. G., 2006, ApJ, 646, 420
Prestwich A. H. et al., 2007, ApJ, 669, L21
Remillard R. A., McClintock J. E., 2006, ARA&A, 44, 49
Rutten R. G. M., van Paradijs J., Tinbergen J., 1992, A&A, 260, 213
Scott D. W., 1992, Multivariate Density Estimation. Wiley, New York
Silverman J. M., Filippenko A. V., 2008, ApJ, 678, L17
Singh N. S., Naik S., Paul B., Agrawal P. C., Rao A. R., Singh K. Y., 2002, A&A, 392, 161
Tuthill P. G., Monnier J. D., Lawrance N., Danchi W. C., Owocki S. P., Gayley K. G., 2008, ApJ, 675, 698

Table A1. Parameters for known BH-HMXBs.

Name	Type	$R_\star$ (R$_\odot$)	P_o (h)	$M_\star$ (M$_\odot$)	M_{BH} (M$_\odot$)	$v_\star \sin(i)$ (km s^{-1})	$v_{BH}\sin(i)$ (km s^{-1})	i (°)	T_E (h)	Φ_E phase	$a_1 + a_2$ (R$_\odot$)	R_S (R$_\odot$)	T_P (h)	Refs
IC 10 X-1 (1)	WR	2	34.9	35	32	370	404.7	90	5.24	0.15	22.29	10.5	1.00	a, b, c
IC 10 X-1 (2)	WR	1.5	34.9	17	23	370	273.5	90	5.24	0.15	18.52	8.7	0.90	a, b, c
IC 10 X-1 (3)	WR	2	34.9	35	32	370	404.7	70	5.24	0.15	23.72	11.2	0.94	a, b, c
IC 10 X-1 (4)	WR	1.5	34.9	17	23	370	273.5	70	5.24	0.15	19.70	9.3	0.85	a, b, c
NGC 300 X-1	WR	1.8	32.0	26	20	267	347.1	65	6.40	0.20	17.86	11.2	1.03	d, e
M33 X-7	O	19.6	82.8	70	15.65	108.9	487.1	74.6	12.19	0.15	42.17	19.5	12.25	f
LMC X-1	O	17	93.8	32	11	71.6	208.3	36.4	Not eclipsing	NA	36.45	–	–	g
LMC X-3	B5V	4.5	40.92	3.7	6.95	240	127.77	69.6	Not eclipsing	NA	13.23	–	–	h, i
Cyg X-1	O	16.2	134.37	14.8	19.2	70	53.958	27.1	Not eclipsing	NA	30.12	–	–	j
NGC 4490	WR?	1.5	6.4	–	–	–	–	–	Not eclipsing?	NA	–	–	–	k
Cyg X-3	WR	1	4.8	10.3	2.4	109	469	43	Not eclipsing?	NA	3.35	–	–	l, m

Notes. A 'most massive' and 'least' massive scenario are considered for IC 10 X-1, along with two cases for the inclination.
References: a – Silverman & Filippenko (2008); b – Prestwich et al. (2007); c – this work; d – Carpano et al. (2007); e – Crowther et al. (2010); f – Orosz et al. (2007); g – Orosz et al. (2009); h – Val-Baker, Norton & Negueruela (2007); i – Orosz et al. (2014); j – Orosz et al. (2011); k – Esposito et al. (2013); l – Zdziarski, Mikołajewska & Belczyński (2013); m – Singh et al. (2002). The following are computed from reported data: $v_{BH}\sin(i)$, $a_1 + a_2$, R_S (radius of X-ray shadow), T_P (predicted duration of eclipse by companion).

Tutukov A. V., Fedorova A. V., Cherepashchuk A. M., 2013, Astron. Rep., 57, 657

Val-Baker A. K. F., Norton A. J., Negueruela I., 2007, in Antonelli L. A. et al., eds, AIP Conf. Proc. Vol. 924, The Multicoloured Landscape of Compact Objects and Their Explosive Origins. Am. Inst. Phys., New York, p. 530

Valsecchi F., Glebbeek E., Farr W. M., Fragos T., Willems B., Orosz J. A., Liu J., Kalogera V., 2011, in Schmidtobreick L., Schreiber M. R., Tappert C., eds, ASP Conf. Ser. Vol. 447, Evolution of Compact Binaries. Astron. Soc. Pac., San Francisco, p. 271

Wang Q. D., Whitaker K. E., Williams R., 2005, MNRAS, 362, 1065

Wilson C. D., Welch D. L., Reid I. N., Saha A., Hoessel J., 1996, AJ, 111, 1106

Zdziarski A. A., Mikołajewska J., Belczyński K., 2013, MNRAS, 429, L104

APPENDIX A:

We performed calculations of the type presented in Section 5.1 for IC 10 X-1 and the known BH-HMXBs, whose properties are summarized below; the results (measured eclipse durations versus predicted) are shown in Table A1.

NGC 300 X-1 is a WR BH-HMXB with orbital period P_{orbit} = 1.33 d (32 h), and an X-ray eclipse duration of about 0.2 in phase (6 h) as seen in fig. 5 of Carpano et al. (2007). Our inferred radius for the shadowing body (11 M$_\odot$) is very similar to that for IC 10 X-1. The observed X-ray shadow is again ∼5 times larger than the eclipse duration expected for the companion. Close similarities between the two systems' mass, mass ratio, companion type, and X-ray spectrum have been noted (e.g. Crowther et al. 2010).

M33 X-7 is a SG BH-HMXB (Orosz et al. 2007) with an orbital period of P_{orbit} = 3.45 d (82.8 h) having 12 h long eclipses (0.147 phase duration). Unlike the WR systems in Table A1 its X-ray eclipse duration closely matches the anticipated radius of its O SG companion.

CXOU J123030.3+413853 in NGC 4490 is a candidate WR BH-HMXB (Esposito et al. 2013) with a very short orbital period of just 6.4 h (0.267 d). Its X-ray light curve appears more sinusoidal than step like, suggesting it is not eclipsing. The companion has not been identified owing to its great distance, so no RV curve is available, however, given the short orbital period (and consequently small separation) the inclination must be very low to avoid eclipses.

LMC X-1 is a non-eclipsing SG system. Its X-ray light curve is nonetheless strongly modulated, and is close to a cosine function with respect to orbital phase (Orosz et al. 2009).

LMC X-3 is a non-eclipsing system with a B3V companion. Its relatively high inclination implies that the wind does not present the wide high-opacity/scattering shadow seen in the WR (and to a lesser extent the SG) systems.

Cyg X-3 is a non-eclipsing WR BH-HMXB with a 4.8 h (0.2 d) orbit showing strong sinusoidal-like X-ray modulation. Extensive X-ray observations by Singh et al. (2002) reveal the orbital period derivative is $\frac{\dot{P}}{P} = 1.05 \times 10^{-6}$ yr^{-1}.

SUPPORTING INFORMATION

Additional Supporting Information may be found in the online version of this article:

(http://mnras.oxfordjournals.org/lookup/suppl/doi:10.1093/mnras/stu2151/-/DC1).

Please note: Oxford University Press are not responsible for the content or functionality of any supporting materials supplied by the authors. Any queries (other than missing material) should be directed to the corresponding author for the article.

This paper has been typeset from a TEX/LATEX file prepared by the author.